PAPER

Local properties of magnetic reconnection in nonlinear resistive- and extended-magnetohydrodynamic toroidal simulations of the sawtooth crash

To cite this article: M T Beidler *et al* 2017 *Plasma Phys. Control. Fusion* **59** 025007

Local properties of magnetic reconnection in nonlinear resistive- and extended-magnetohydrodynamic toroidal simulations of the sawtooth crash

M T Beidler[1,3]**, P A Cassak**[1]**, S C Jardin**[2]** and N M Ferraro**[2]

[1] Department of Physics and Astronomy, West Virginia University, Morgantown, WV 26506, USA
[2] Princeton Plasma Physics Laboratory, Princeton, NJ 08543, USA

E-mail: beidler@wisc.edu

Abstract

We diagnose local properties of magnetic reconnection during a sawtooth crash employing the three-dimensional toroidal, extended-magnetohydrodynamic (MHD) code M3D-C^1. To do so, we sample simulation data in the plane in which reconnection occurs, the plane perpendicular to the helical $(m, n) = (1, 1)$ mode at the $q = 1$ surface, where m and n are the poloidal and toroidal mode numbers and q is the safety factor. We study the nonlinear evolution of a particular test equilibrium in a non-reduced field representation using both resistive-MHD and extended-MHD models. We find growth rates for the extended-MHD reconnection process exhibit a nonlinear acceleration and greatly exceed that of the resistive-MHD model, as is expected from previous experimental, theoretical, and computational work. We compare the properties of reconnection in the two simulations, revealing the reconnecting current sheets are locally different in the two models and we present the first observation of the quadrupole out-of-plane Hall magnetic field that appears during extended-MHD reconnection in a 3D toroidal simulation (but not in resistive-MHD). We also explore the dependence on toroidal angle of the properties of reconnection as viewed in the plane perpendicular to the helical magnetic field, finding qualitative and quantitative effects due to changes in the symmetry of the reconnection process. This study is potentially important for a wide range of magnetically confined fusion applications, from confirming simulations with extended-MHD effects are sufficiently resolved to describe reconnection, to quantifying local reconnection rates for purposes of understanding and predicting transport, not only at the $q = 1$ rational surface for sawteeth, but also at higher order rational surfaces that play a role in disruptions and edge-confinement degradation.

Keywords: fusion, magnetic reconnection, sawteeth

(Some figures may appear in colour only in the online journal)

1. Introduction

During a cycle of the sawtooth crash, the temperature of the core plasma in a tokamak slowly rises (for a few ms) followed by a rapid crash down (10–100 s of μs). The edge temperature concomitantly undergoes a slow decline followed by a rapid increase. It was discovered in 1974 in the symmetric Tokamak (ST) [1] and shortly thereafter a qualitative explanation appeared involving the change of magnetic topology during magnetic reconnection at the $q = 1$ rational surface [2]. The Kadomtsev picture is generally accepted although it does not explain the trigger mechanism, crash time, or measured evolution of q_0, and other explanations have also been put

---

[3] Beidler's current affiliation: Department of Engineering Physics, University of Wisconsin, Madison, WI 53706, USA.

forward [3]. Sawtooth phenomena need to be better understood in order to fully optimize ITER operation [4]. If natural sawteeth are deemed to be too deleterious, operational regimes exist where smaller amplitude sawteeth can be triggered by RF [5], or eliminated entirely as in the 'hybrid' regimes [6–8].

There are many undesirable ramifications of sawteeth. Sawtooth events degrade confinement of fusion alpha particles generated in the core of the tokamak, limiting their ability to transfer their energy to the plasma. It was recently argued that fast-ion transport strongly depends on the crash time [9]. The sawtooth crash forms seed islands on higher-order rational surfaces, which can destabilize neoclassical tearing modes (NTMs) [10]. Because NTMs often lead to locked mode disruptions (e.g. [11]), sawteeth are also responsible for triggering disruptions in some circumstances.

Despite its importance, a predictive capability of sawteeth and its effects has been elusive. There remains no accepted model of the crash time. In early devices, crash times were consistent with the time it takes resistive (Sweet–Parker) reconnection to process all available magnetic flux [2], and early simulations [12, 13] were largely consistent with this picture. However, the crash time was much quicker than the prediction for sawteeth at the Joint European Torus [14] and in the Tokamak Test Fusion Reactor [15]. It has been proposed that this discrepancy is due to collisionless reconnection being faster than collisional reconnection in the hotter devices [16]. However, predicting the crash time is more complicated than only including collisionless reconnection effects, primarily because reconnection does not always continue long enough to process all available magnetic flux in the core, i.e., reconnection can be incomplete [15]. What causes reconnection to be incomplete and what sets the time scale at which reconnection ceases remain open questions. The limited understanding of incomplete reconnection impacts tokamak transport modeling. Low-dimensional transport models capture the sawtooth period and amplitude [17], but the fraction of flux reconnected is an input parameter rather than self-consistently calculated (e.g., [18]).

Models for incomplete reconnection often discuss local physics at the reconnection site [19–23]. Therefore, achieving the long-term goal of understanding how reconnection occurs in toroidal fusion devices and using this to develop first-principles predictions of tokamak plasma evolution requires an ability to study local aspects of reconnection in toroidal geometry. Since collisionless physics is a candidate for describing the reconnection rate, toroidal extended-magneto-hydrodynamic (MHD) or kinetic codes are needed to properly analyze the magnetic reconnection. Generally, extended-MHD models retain physics past that of resistive-MHD, including two-fluid effects and more physical closures for conductivity and viscosity. It has been only recently that extended-MHD terms have been integrated into fluid codes that employ a toroidal geometry.

There are previous studies employing extended-MHD physics in both cylindrical and toroidal 3D geometries. Incomplete reconnection was reported in toroidal simulations with extended-MHD physics [24] using the M3D code [25]

with ion diamagnetic terms included. While it was not concluded whether the incomplete reconnection was due to the inclusion of extended-MHD effects or a consequence of the lesser energy of the second crash, it is the first simulation showing incomplete reconnection in a 3D toroidal geometry. More recent sawtooth simulations have also been run with extended-MHD physics [26, 27] using the TM1 code [28]. These simulations employ a large aspect ratio approximation (periodic cylinder) with a circular cross-section and a constant equilibrium density profile with cold ions and anomalous electron viscosity. With these assumptions, they showed that using typical parameters from the axially symmetric divertor experiment-upgrade (ASDEX-U) tokamak, simulations gave sawtooth crash time scales that were comparable to experimental observations, although the trigger mechanism, sawtooth period, and comparison of the change in q_0 with experiments were not addressed.

A complication in studying the reconnection process in toroidal numerical simulations is that it is easiest to analyze the simulation data in poloidal planes, while it has been known since early work (e.g. [2]) that the plane in which reconnection occurs is normal to the helical magnetic field, which is not the same as the toroidal plane. We note that in a general 3D magnetic geometry reconnection is not confined to a plane (e.g. [29]), but in the limit of a strong helical magnetic 'guide field', a 'reconnection plane' can be defined in the vicinity of the reconnection site. We are unaware of any studies of 3D toroidal simulations to find the appropriate plane of reconnection. Developing a set of tools to do so and performing a preliminary analysis is a major goal of this study.

A second goal of the present study is repeating this process at multiple toroidal locations to study the dependence on toroidal angle of sawtooth phenomena. Viewing data from a single toroidal angle misses out on important information on how the mode evolves. It was not until the WT-3 tokamak in the early 2000s that multiple soft x-ray detector arrays were placed around the device at different toroidal angles [30]. On WT-3, detector arrays were positioned at $\phi = 0°$, $90°$, and $202.5°$.

For the WT-3 discharges, the plasma current was directed opposite to the toroidal magnetic field, giving the reconnection mode a counter-clockwise helical polarity. With a tangential neutral beam causing rotation parallel to the toroidal field, the mode was observed to rotate in the clockwise poloidal direction. It was also observed that the hot core was shifted toward the outboard side for all toroidal locations. Furthermore, it was apparent that the poloidal location of reconnection affects the structure of the electron temperature. When the hot core was offset towards the outboard side, the electron temperature profile elongated along the $q = 1$ surface.

In this study, we develop an approach to find the reconnection plane in 3D toroidal simulations. To view data local to the reconnection site, we employ a novel method to sample data between computational grid points in the toroidal direction. The methodology should be effective across codes and numerical models, including kinetic modeling. We use

this approach both on resistive- and extended-MHD physics models, using the M3D-C^1 code. In doing so, we are able to make direct comparisons of the local reconnection physics in both systems. We find, as expected, that the collisional reconnection process is much slower than reconnection in well-resolved extended-MHD. We find the contributions to Ohm's law in the reconnection plane and compare the measured reconnection rates to theoretical predictions. We also present the first known identification of the quadrupole out-of-plane Hall magnetic field that is an indicator of two-fluid effects in 3D toroidal simulations. We then compare properties of the reconnection at different toroidal angles.

In section 2, we describe the simulations in this study. In section 3, we examine the simulations holistically using data from the poloidal plane. Then, we describe the approach to finding the reconnection plane in section 4.1. We discuss local properties of reconnection in the reconnection plane in section 4. Section 5 discusses how reconnection varies at different toroidal locations. We conclude and discuss applications in section 6.

2. Numerical simulation setup

2.1. The M3D-C^1 code

We use the M3D-C^1 code [31] to evolve the extended-MHD equations for the density n, velocity $\mathbf{v}$, ion and electron pressure p_i and p_e, and magnetic field B:

$$\frac{\partial n}{\partial t} + \nabla \cdot (n\mathbf{v}) = 0, \tag{1}$$

$$nM_\mathrm{i}\left[\frac{\partial \mathbf{v}}{\partial t} + \mathbf{v} \cdot \nabla \mathbf{v}\right] + \nabla p - \mathbf{J} \times \mathbf{B} = -\nabla \cdot \mathbf{\Pi}_\mu - \nabla \cdot \mathbf{\Pi}_\mathrm{GV}, \tag{2}$$

$$\frac{3}{2}\left[\frac{\partial p_\mathrm{e}}{\partial t} + \nabla \cdot (p_\mathrm{e}\mathbf{v})\right] + p_\mathrm{e}\nabla \cdot \mathbf{v} = \eta J^2 - \nabla \cdot \mathbf{q}_\mathrm{e}, \tag{3}$$

$$\frac{3}{2}\left[\frac{\partial p_\mathrm{i}}{\partial t} + \nabla \cdot (p_\mathrm{i}\mathbf{v})\right] + p_\mathrm{i}\nabla \cdot \mathbf{v} = -\mathbf{\Pi}_\mu : \nabla \mathbf{v} - \nabla \cdot \mathbf{q}_\mathrm{i}, \tag{4}$$

$$\frac{\partial \mathbf{B}}{\partial t} = -\nabla \times \mathbf{E}. \tag{5}$$

In these equations, $\mathbf{J} = \nabla \times \mathbf{B}/\mu_0$ is the current density, the electric field is given by the generalized Ohm's law as

$$\mathbf{E} + \mathbf{v} \times \mathbf{B} = \eta\mathbf{J} + \frac{1}{ne}(\mathbf{J} \times \mathbf{B} - \nabla p_\mathrm{e}), \tag{6}$$

and M_i is the ion mass. The Braginskii gyroviscosity pressure tensor $\mathbf{\Pi}_\mathrm{GV}$ [32] can be included in equation (2). A generic isotropic viscous term can be included, given by $\mathbf{\Pi}_\mu = -\mu(\nabla \mathbf{v} + \nabla \mathbf{v}^\mathrm{T})$, where μ is an arbitrary scalar field and $\nabla \mathbf{v}^\mathrm{T}$ is the matrix transpose of $\nabla \mathbf{v}$. The resistivity η has a Spitzer form given by $\eta = \eta_r + \eta_0/T_\mathrm{e}^{3/2}$. For the pressure evolution, the ratio of specific heats for both species is set to 5/3, and electron and ion heat fluxes are given by $\mathbf{q}_\mathrm{e,i} = -\kappa_0\nabla T_\mathrm{e,i} - \kappa_\parallel\mathbf{b}\mathbf{b} \cdot \nabla T_\mathrm{e,i}$, where $\kappa_0 = \kappa_\mathrm{iso}p/T_\mathrm{e}^{3/2}$

describes isotropic conduction and $\kappa_\parallel$ is for parallel conduction, where κ_iso is a constant. Electrons are assumed massless for simplicity. The code can simulate different physical models: ideal-MHD with equations (1) and (5), and the terms on the left side of the equality in equations (2), (3), (4), and (6); resistive-MHD with the first term on the right side of the equality in equations (2) and (6), and all terms on the right side of the equality in equations (3) and (4) included as well; and extended-MHD including all the terms.

For representing the variables spatially, M3D-C^1 has 3D finite elements with continuous first derivatives between elements. In the poloidal plane, M3D-C^1 uses a reduced-quintic (fourth order polynomial with additional constrained coefficients) representation for the solution on an unstructured triangular grid. Toroidally, it has a Hermite cubic polynomial representation. This gives the elements a triangular prism shape. If the average length of an element edge in the poloidal plane is Δx, the reduced-quintic representation has an error on the order of $(\Delta x)^5$ (see [33]). For the simulations included in this study, we employ a semi-implicit time stepping method to evolve the model equations; implicit schemes allow for time steps much larger than the Courant–Friedrichs–Lewy condition constraining the time step in explicit methods.

M3D-C^1 uses a cylindrical coordinate system (R, ϕ, Z). The positive direction of ϕ is counter-clockwise looking down from the top of the torus. For a plasma current parallel to the toroidal magnetic field in the positive ϕ direction, the resulting helical field has a clockwise helicity relative to the ϕ-direction. R is the major radial direction from the azimuthal axis, and Z is the vertical direction.

The boundary conditions employed in the 3D toroidal simulations are as follows. The flow $\mathbf{v}$ has 'no-slip' boundary conditions (the flow tangential to the boundaries is held constant). There is no flow into the boundary, i.e., $\hat{\mathbf{n}} \cdot \mathbf{v} = 0$ where $\hat{\mathbf{n}}$ is the unit vector normal to the boundary. The normal and toroidal magnetic fields have Dirichlet boundary conditions $\hat{n} \cdot \mathbf{B} = \hat{\phi} \cdot \mathbf{B} = \mathrm{constant}$, and the poloidal magnetic field B_θ has Neumann boundary conditions $\hat{\mathbf{n}} \cdot \nabla B_\theta = \mathrm{constant}$. The plasma parameters n, p, and T are all held constant on the boundary.

M3D-C^1 represents the velocity $\mathbf{v}$, magnetic vector potential $\mathbf{A}$, and magnetic field $\mathbf{B}$ in terms of scalar variables $\Phi, \omega, \chi, \psi, f$ as [34]:

$$\mathbf{v} = R\nabla\Phi \times \hat{\phi} + R\omega\hat{\phi} + \frac{1}{R^2}\nabla_\perp\chi, \tag{7}$$

$$\mathbf{A} = R\hat{\phi} \times \nabla f + \frac{\psi}{R}\hat{\phi} - F_0\ln R\hat{Z}, \tag{8}$$

$$\mathbf{B} \equiv \nabla \times \mathbf{A} = \frac{1}{R}\nabla\psi \times \hat{\phi} - \nabla_\perp\frac{\partial f}{\partial \phi} + \frac{F}{R}\hat{\phi}, \tag{9}$$

where $\nabla_\perp$ is the del operator in the $R - Z$ plane. For the representation of the velocity, Φ is the stream-function describing incompressible flow in the poloidal plane, ω is the toroidal angular frequency, and χ captures the effect of compressible flow in the poloidal plane. This form allows the numerical method evolving the scalar variables to

Table 1. Parameters used to solve the Grad–Shafranov equation, which determine the equilibrium used to initialize the simulations with the M3D-C^1 code.

Parameter	I_p	q_0	B_0	p_0	$p_{0,i}$	p_{edge}	n_0	expn
Value	0.8	0.6	1.0	0.006	0.003	0.0003	1.0	0.2

approximately separate the physics of the Alfvén and fast and slow magnetosonic waves for the toroidal system with a strong B_ϕ field [35]. For the magnetic field representation, ψ is the magnetic flux function describing the magnetic field in the poloidal plane and $F = F_0 + R^2 \nabla \cdot \nabla_\perp f$ is an auxiliary variable. F_0 is a constant proportional to the current in the (modeled) toroidal field magnets. The gauge condition implied by this representation is $\nabla_\perp \cdot (R^{-2}\mathbf{A}) = 0$.

The system of units for all quantities appearing hereafter is derived from a characteristic length, density, and magnetic field of $L_{norm} = 1$ m, $n_{norm} = 10^{20}$ particles m^{-3}, and $B_{norm} = 1$ T. This sets the normalization for velocity to $v_{norm} = B_{norm}/(\mu_0 n_{norm} M_i)^{1/2} = 2.2 \times 10^6$ m s^{-1}, the Alfvén speed based off the characteristic magnetic field and density for hydrogen, the time to $t_{norm} = L_{norm}/v_{norm} = 0.46$ μs, the pressure to $p_{norm} = B_{norm}^2/2\mu_0 = 3.9$ atm, the electric field to $E_{norm} = v_{norm}B_{norm} = 2.2 \times 10^6$ V m^{-1}, and the current density to $J_{norm} = B_{norm}/\mu_0 L_{norm} = 0.80$ MA m^{-2} (implying the current is normalized to $I_{norm} = 0.80$ MA). The resistivity is normalized to $\eta_{norm} = \mu_0 L_{norm} v_{norm} = 2.8$ Ohm m, the viscosity to $\mu_{norm} = n_{norm} M_i L_{norm} v_{norm} = 0.37$ kg m^{-1} s^{-1}, and conductivity to $\kappa_{norm} = k_B n_{norm} L_{norm} v_{norm} = 2.2 \times 10^{26}$ W m^{-1} deg(K)$^{-1}$, where k_B is the Boltzmann constant. The terms in equations (2) and (6) that are only used in the extended-MHD model are scaled by a constant $d_b = d_i/L_{norm}$, where d_i is the ion inertial scale c/ω_{pi}. This allows the user to specify the strength of two-fluid effects.

2.2. Initialization and optimization

The simulations are initialized using an axisymmetric equilibrium determined from solving the Grad-Shafranov equation [36, 37] using a module included in M3D-C^1. The solver assumes the magnetic field and gas pressure profiles have a polynomial form, and a relaxation technique is employed to approach the exact solution. Input parameters include the toroidal plasma current I_p, the central safety factor q_0 and toroidal magnetic field B_0, the central total and ion pressures p_0 and $p_{0,i}$, the total edge pressure p_{edge}, central density n_0, and a variable named 'expn' to set the density profile from the pressure profile as $n = p^{expn}$. Values used to generate the equilibrium for this study are given in table 1 and profiles through the midplane at $Z = 0$ are shown in figure 1. The equilibrium generated for this set of inputs has a plasma column with an outer boundary parametrized by $R(\theta) = 3.20 + \cos[\theta + 0.2\sin(\theta)]$, $Z(\theta) = 1.3\sin(\theta)$, where θ is the poloidal angle. This configuration has a magnetic axis with radius $R_0 = 3.28$ m, where the $q = 1$ rational surface is located at a minor radius of approximately $r_1 = 0.59$ m. We note that this equilibrium does not
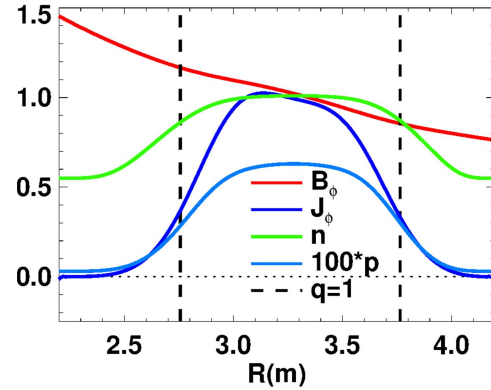
Figure 1. Equilibrium profiles of normalized system parameters through the midplane at $Z = 0$, which are used throughout all simulations.

correspond to a particular tokamak, but is instead chosen to study the basic physics of reconnection in sawteeth.

Optimizing parameters in the fully nonlinear extended-MHD model in a 3D toroidal geometry is challenging because run times are long, so we use M3D-C^1 simulations in its 2D axisymmetric nonlinear, 3D linear, and 3D resistive-MHD forms to optimize parameters. This allows us to run a series of computationally inexpensive simulations to probe the equilibrium parameter space, spatial and time resolution. It also allows us to tune the simulated plasma controllers for plasma density and current, which includes applying a loop voltage by ramping the poloidal flux at the boundary to maintain the plasma current.

The chosen finite element grid in each poloidal plane of the computational domain is shown in figure 2(a). The average edge of an element is 0.04 m, as seen in the zoomed-in panel (b). There are 16 toroidal planes, each with identical poloidal meshes. All the DOFs are located at the nodes of the triangular prisms. There are 12 DOF at each node associated with each scalar variable. The split-implicit method first advances all 3 velocity variables (36 DOF at each node) implicitly, and then uses these to advance the magnetic, pressure, and density variables. The sparse matrix equations are solved using the PETSc GMRES iterative solver with a block-Jacobi preconditioner [38].

The resolution is chosen by running multiple toroidal, nonlinear resistive-MHD simulations where we vary the resolution while keeping all other parameters constant. We check that there is no qualitative change in the solution. In the nonlinear extended-MHD model, the system of equations to be solved is much more complex than that of the resistive-MHD case. Because the iterative solver employed has a limit on the number of loops for solving each time slice, the maximum time step that could be used was limited by a factor
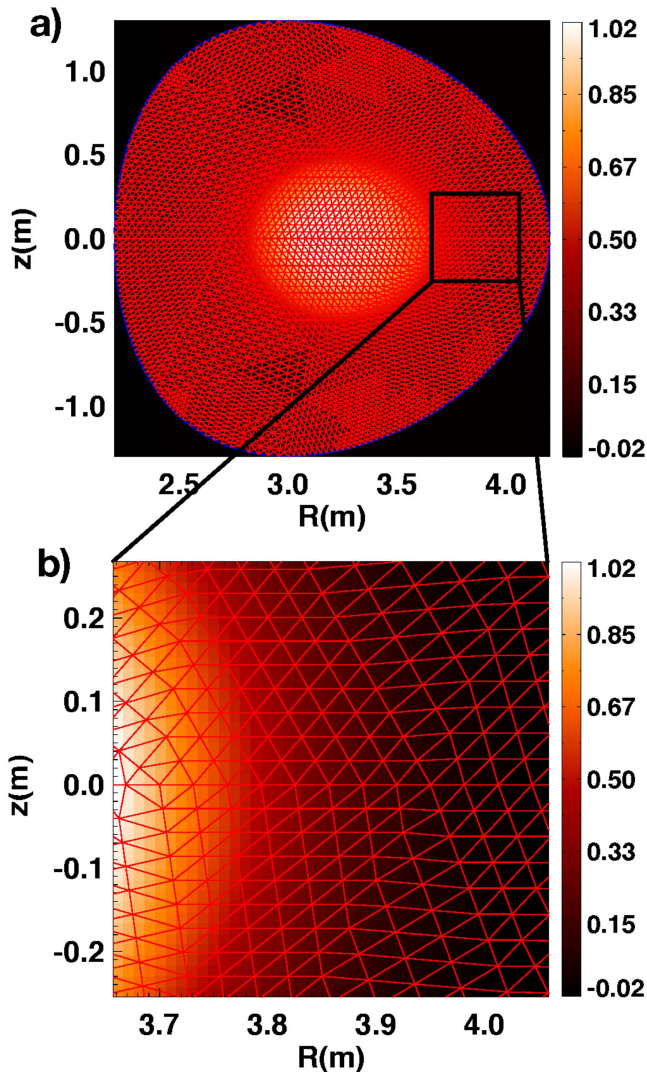
Figure 2. (a) View of the toroidal current density at a constant toroidal angle over-plotted with the triangular finite element mesh. (b) Zoomed in portion of the domain in (a) to show the resolution of the mesh, with an average edge length of 0.04 m.

of ~10 smaller than for the resistive-MHD simulations. This restricted our ability to parametrically scan the resolution for the nonlinear extended-MHD simulations, and will be a part of future studies. However, the results of this study summarized in the next few sections serve as additional evidence that the grid resolution is sufficient.

After setting the equilibrium, a small random perturbation on the poloidal flow on the order of $0.1c_{A\theta}$ is employed to initialize the system, where $c_{A\theta}$ is the Alfvén speed based on the poloidal magnetic field. The magnitude of the initial perturbation is varied to ensure the resulting evolution is not sensitive to it. The timestep is optimized in 2D and 3D resistive simulations, with $20t_{norm}$ being the largest timestep that could be used where the results are qualitatively consistent with simulations with a lower timestep. The extended-MHD simulations are performed with the largest timestep that the iterative solver could converge, which is $2t_{norm}$.

A simulated neutral beam is included as a source of particles, torque, and energy into the system. This beam has a finite deposition area and is located in the central region near the magnetic axis. It is set to have a beam voltage of 10^4 V, deposit ions at a rate of 5×10^{22} per second, and have a Gaussian profile of width 0.8. The simulations also use a spatially varying pellet fueling source in the continuity equation equal to $P_{rate} \times n_0 (p/p_0)^{expn}$, where p is the local pressure and P_{rate} is the pellet rate equal to 3×10^{-5} per second. A density controller is used to hold the number of particles at 8.8×10^{20} and a current controller is used to hold I_p at $0.8 I_{norm}$, both using a standard proportional-integral-derivative feedback control [31]. With these sources and controls, we find a range of perpendicular and parallel thermal conductivities that do not qualitatively alter the evolution by running simulations with the 2D nonlinear version of the code. We choose $\kappa_{iso} = 4.0 \times 10^{-6}$ and $\kappa_{\parallel} = 10$. Additionally, we set the viscosity to $\mu = 3.058 \times 10^{-5}$.

A key aspect of this study is resolving two-fluid physics. To ensure we resolve the Hall scales, we use the 3D linear version of the code. The system of equations is expanded using $A = A_0 + A_1$, where A_0 is the equilibrium value and A_1 is the complex perturbation, and A represents all dynamical variables. Keeping only the linear terms and Fourier transforming in ϕ, the toroidal derivatives are replaced by a multiplier of in, with n being the chosen number of the toroidal mode. Employing these linear simulations for a single n mode at a time, we hold the two-fluid parameter d_b constant and change the resistivity, and vice versa. We choose values of the resistivity of $\eta \sim 1.5 \times 10^{-6}$ at the $q = 1$ surface and the two-fluid parameter $d_b = 0.1$. For these simulations, the grid sufficiently resolves the resistive reconnection layer in resistive-MHD simulations ($d_b = 0$) for $n = 0$, 1 and 2, and when extended-MHD effects are turned on the resistivity is small enough that the two-fluid effects dominate. Note, for $d_b = 0.1$, the ion inertial scale is $d_i = 10$ cm, rather than the value based on the normalized density n_{norm} of 2.28 cm.

3. Macroscopic properties

The nonlinear 3D simulations are allowed to evolve in time from the linear through to the nonlinear phase. Before finding the reconnection plane, we look at macroscopic properties of the simulation results. We begin by comparing results from resistive-MHD and extended-MHD simulations. The grid and the initial conditions of the two simulations are identical; the only difference between the two simulations is the presence of extended-MHD terms and a smaller timestep in the extended-MHD simulations. A complete sawtooth crash is observed in each simulation.

First, we compare the kinetic energy contained in the lowest order toroidal modes. In figure 3, the evolution of the kinetic energy KE in different toroidal modes is shown for the (a) resistive-MHD ($d_b = 0$) and (b) extended-MHD ($d_b = 0.1$) simulations, where the red stars indicate the approximate beginning of the reconnection, or crash, phase in each respective sawtooth cycle. The first striking difference between the two is the disparity in the time scales; the extended-MHD simulation evolves from $t = 0$ to its
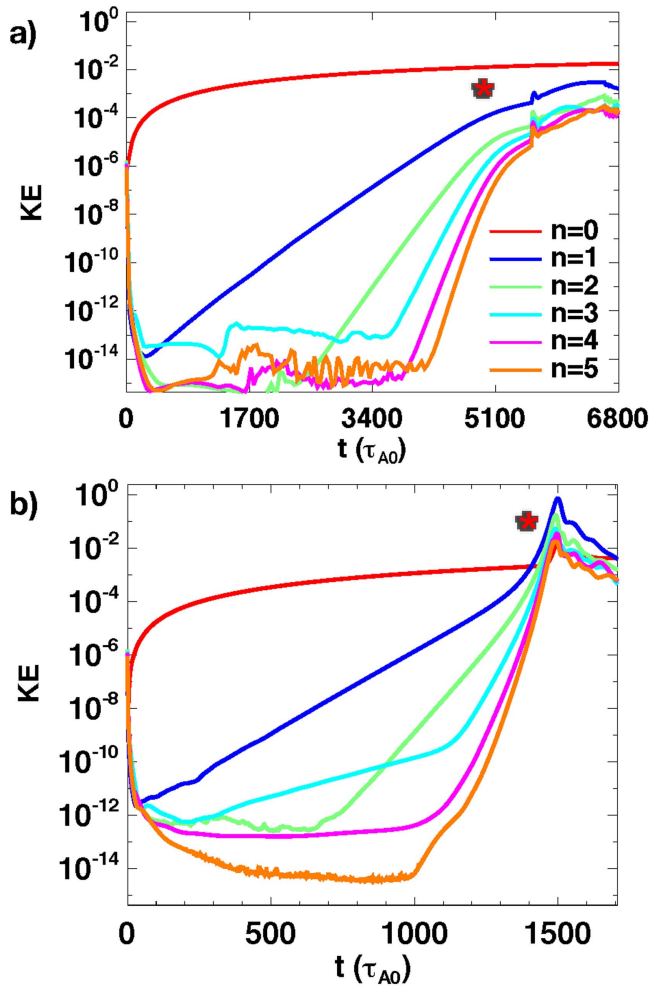
Figure 3. Kinetic energy in toroidal modes $n = 0 - 5$ in (a) resistive-MHD and (b) extended-MHD simulations as a function of time t. The (red) stars indicate the approximate beginning of the reconnection, or crash, phase in each respective sawtooth cycle. Time scales are much faster in extended-MHD, and there is late nonlinear acceleration of the growth for the extended-MHD case compared to deceleration in the resistive case.

Figure 4. Poloidal cross-sections of the electron temperature during the reconnection phase of the sawtooth crash for the resistive-MHD simulation. White x's show the location of the reconnection site determined from Poincaré plots. The counter-clockwise poloidal drift is due to the external neutral beam adding torque to the system and causing the helical mode to rotate toroidally.

Figure 5. Poloidal cross-sections of the electron temperature as in figure 4, but for the extended-MHD simulation. The time scale of the core expulsion is ~15 times shorter than for the resistive simulation.

maximum kinetic energy in roughly a quarter of the time it takes in resistive-MHD. The calculated growth rate of the kinetic energy in the $n = 1$ toroidal mode is ~0.005 for the resistive case and ~0.015 for the extended-MHD case.

A second important observation in figure 3 is the non-linear acceleration of the kinetic energy growth rates for the extended-MHD simulation from $t \sim 1400 - 1500$ consistent with [16], and a deceleration of the mode growth for the resistive simulation after $t \sim 5000$. This implies that reconnection is not only faster using extended-MHD, but also increases in rate as the reconnection phase proceeds, while resistive-MHD has slower reconnection that slows even further during the crash. The acceleration of the mode growth rate is similar to results from [39], where reduced, extended-MHD simulations showed an accelerating growth rate during the reconnection phase across a parameter space of poloidal beta and density gradient widths. This is also reminiscent of experimental observations from [30] of a two-phase crash,
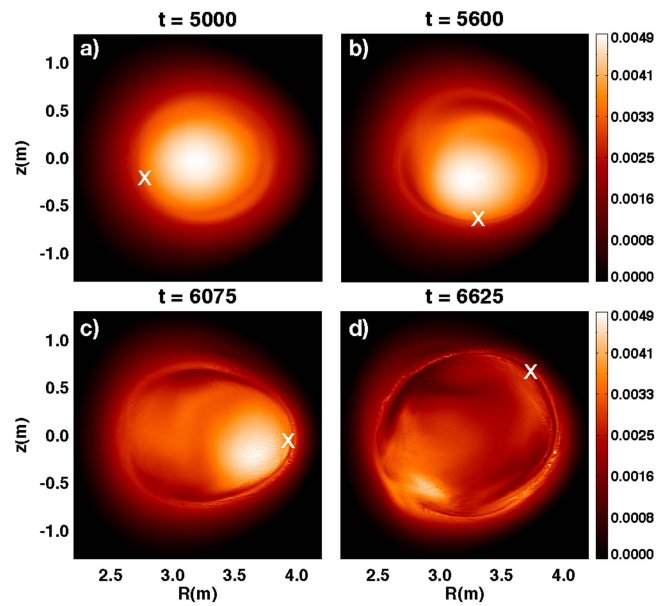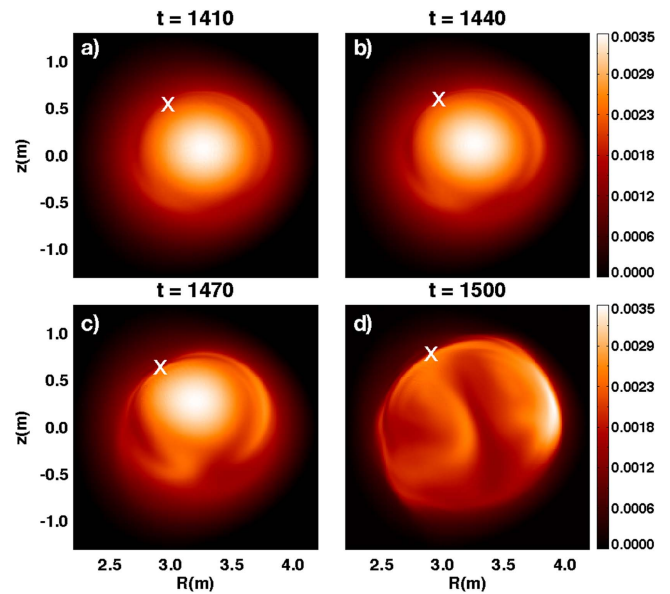
which was composed of a gradually evolving initial phase followed by a rapid phase.

A third important difference between resistive-MHD and extended-MHD is the time it takes for reconnection to process the magnetic fields and expel the hot plasma in the core, the time scale of the sawtooth crash phase. Shown in figures 4 and 5 for the resistive and extended-MHD simulations, respectively, is the electron temperature in the poloidal plane at a constant toroidal angle for different times throughout the

reconnection phase, where the white x's mark the location of the reconnection site as determined from Poincaré plots and poloidal plane velocity data. Reconnection processes the hot core in the extended-MHD simulation in ∼50 μs, which is in line with experimentally observed crash times and approximately 15 times more rapid than in the resistive-MHD simulation, which processes the core in ∼750 μs. This agrees with the extended-MHD results of [26, 27], which were based off of typical ASDEX discharge parameters. Another important ramification of this result is that it serves as an excellent benchmark suggesting the grid in the extended-MHD simulations properly resolved the two-fluid physics.

Another difference between figures 4 and 5 is the poloidal drift of the reconnection site in the counter-clockwise poloidal direction for the resistive case, while it is not prominent for the extended-MHD case. The torque imparted by the simulated neutral beam causes the helical mode to rotate in the positive toroidal direction, which appears as a counter-clockwise poloidal drift of the reconnection site. This is consistent with experimental results [30], although their plasma current I_p was directed opposite to the toroidal field and neutral beam, so they observed rotation in the clockwise poloidal direction. Since the reconnection phase starts much later in the resistive simulation and also evolves over a longer time scale, the toroidal rotation is apparent for this simulation. However, there is much less time for torque to be imparted in the extended-MHD simulation, and because of this, the poloidal drift of the reconnection site due to the neutral beam is not significant. Calculations confirm that the observed poloidal rotation is consistent with the measured toroidal flow in both simulations.

4. Local properties of reconnection in 3D toroidal geometry

Looking at data in the poloidal plane as done in section 3 is sufficient to gain information about the global properties of the reconnection process, but the reconnection plane is necessary to quantitatively diagnose reconnection in a tokamak. Here, we present the first analysis of the reconnection plane in a 3D toroidal geometry. We note that the discussion in this section is limited to the poloidal plane in which the reconnection site is at the inboard of the torus; a comparison of reconnection properties for sites at other toroidal angles will be discussed in section 5.

4.1. Finding the reconnection plane

It has long been known that the reconnection plane should be the auxiliary plane, normal to the helical magnetic field at the point of reconnection on the rational surface. Here, we describe a general approach to find these planes. While the approach works within the toroidal geometry of the simulations, we show an idealized $q = 1$ surface for a cylindrical toroid for illustrative purposes in figure 6. The checkered-green surface represents the $q = 1$ rational surface. The red line is a helical $q = 1$ magnetic field line.
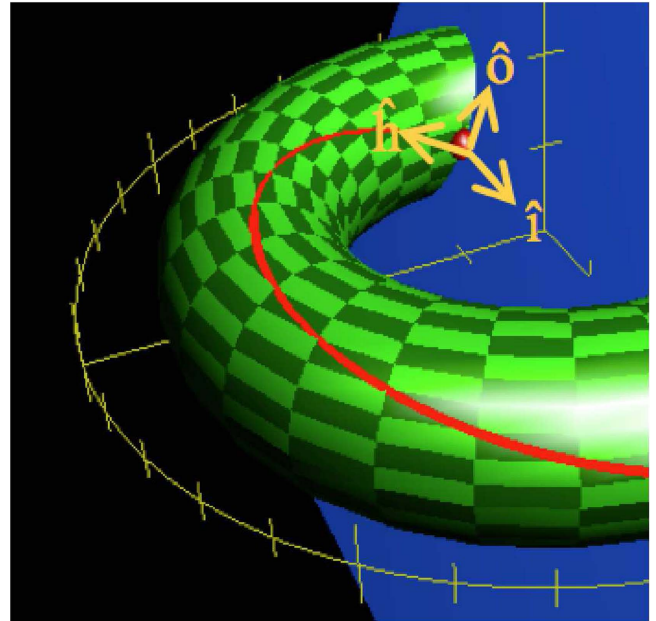

Figure 6. Illustrative example of the approach to find the reconnection plane. The checkered-green circular torus is an idealized $q = 1$ rational surface. The red line is a $q = 1$ magnetic field line. A location of the reconnection site is marked by the red dot. The direction of the local field is $\hat{\mathbf{h}}$, the normal to the $q = 1$ surface (the direction of the reconnection inflow) is $\hat{\mathbf{i}}$, and the reconnection outflow direction $\hat{\mathbf{o}}$ completes the triplet. The reconnection plane (blue) is spanned by $\hat{\mathbf{o}}$ and $\hat{\mathbf{i}}$.

We find the approximate location of the reconnection site (the X-line) using the following procedure. First, we generate Poincaré plots in a chosen poloidal plane to allow us to visually estimate the location of the reconnection site. We expect the pressure gradient to be a maximum at the reconnection site, so we refine the minor radial location of the site in the poloidal plane to match this extremum. The red dot in figure 6 is meant to indicate the location where the reconnection site is found. In the figure, the red dot is on the inboard side of the rational surface. For the initial part of this study, we choose the toroidal angle such that the reconnection site is on the inboard side for simplicity, but the approach in use would work for any toroidal position with the reconnection site at an arbitrary point.

Having an approximate location of the reconnection site in the poloidal plane, we next find the reconnection plane. The vector direction of the local magnetic field at the reconnection site is denoted by $\hat{\mathbf{h}}$ (for 'helical'):

$$\hat{\mathbf{h}} = \hat{\mathbf{b}} = \frac{\mathbf{B}}{|\mathbf{B}|}. \tag{10}$$

It is shown for the illustrative example in figure 6. This unit vector defines the blue plane shown in the figure, which we expect to be the reconnection plane. (We point out that it is not always the case that the reconnection plane is normal to the out-of-plane 'guide' magnetic field [40, 41], but for the tokamak geometry with a large helical field the approximation is expected to be quite good.)

Next we need unit vectors that span the reconnection plane, and the desire is to have them oriented to align with the reconnection inflow and outflow. The inflow direction should be locally normal to the rational surface. To find the normal to the rational surface at the reconnection site, we first define an ancillary unit vector $\hat{t}$ in the poloidal plane that is tangent to the $q = 1$ rational surface. When the reconnection site is at the inboard edge, we simply have $\hat{\mathbf{t}} = \hat{\mathbf{Z}}$ (not shown in figure 6), but for other locations, one merely finds the local direction tangent to the rational surface. Then, the cross product $\hat{\mathbf{t}} \times \hat{\mathbf{h}}$ is normal to both the magnetic field and the $q = 1$ rational surface, which corresponds to the inflow direction. We normalize it and denote it as the inflow direction $\hat{i}$:

$$\hat{\mathbf{i}} \propto \hat{\mathbf{t}} \times \hat{\mathbf{h}}. \tag{11}$$

Finally, the outflow direction, denoted by $\hat{\mathbf{o}}$, completes the triplet:

$$\hat{\mathbf{o}} = \hat{\mathbf{h}} \times \hat{\mathbf{i}}. \tag{12}$$

The i and o directions span the reconnection plane and are expected to be oriented along the reconnection inflow and outflow, as included in the example in figure 6.

With the reconnection plane defined, the plasma parameter data is then obtained on this plane. In the analysis carried out here, we interpolate to find data on a grid rectangular grid of size 200×200 with a separation between data points of order 0.01×0.01, where the exact separation varies slightly depending on the minor radius of the $q = 1$ surface. With this data, we can analyze the properties of reconnection in the reconnection plane.

4.2. Finding the local plasma parameters governing reconnection

We begin by finding the characteristic local plasma parameters governing the local efficiency of the reconnection process, such as the upstream magnetic fields and densities and the aspect ratio of the reconnecting current sheet. In addition to setting the stage for a quantitative analysis of the local reconnection process, this allows us to confirm that the approach used to find the reconnection plane is successful.

The in-plane components of the magnetic field for the extended-MHD simulations are displayed in figure 7, showing (a) the reconnecting magnetic field B_o and (b) the reconnected (normal) magnetic field B_i overlaid with contours of constant ψ_h, consistent with $\vec{B}_\perp = \hat{h} \times \nabla \psi_h$. The color table used here and throughout has white being 0, red positive, and blue negative. The origin has been shifted so that $(o, i) = (0, 0)$ is the reconnection site found with the approach in the previous section. The in-plane field goes to zero at the reconnection site, as it should. This suggests the technique to identify the inflow and outflow directions i and o is appropriate. Furthermore, the polarity of these fields at the origin is consistent with an X-type null, as expected.

Quantifying the local reconnection properties requires measuring the plasma parameters just upstream (in the i direction) of the reconnection site. These quantities are
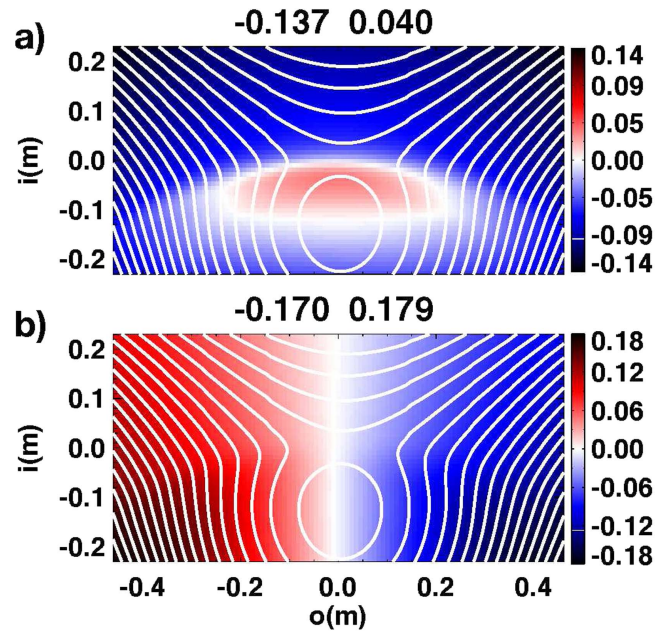

Figure 7. In-plane components of the magnetic fields: (a) B_o and (b) B_i in the reconnection plane for the extended-MHD simulation overlaid with contours of constant ψ_h. The reconnection site is at $(o, i) = (0, 0)$ and the field structure there is consistent with an in-plane X-type magnetic null.
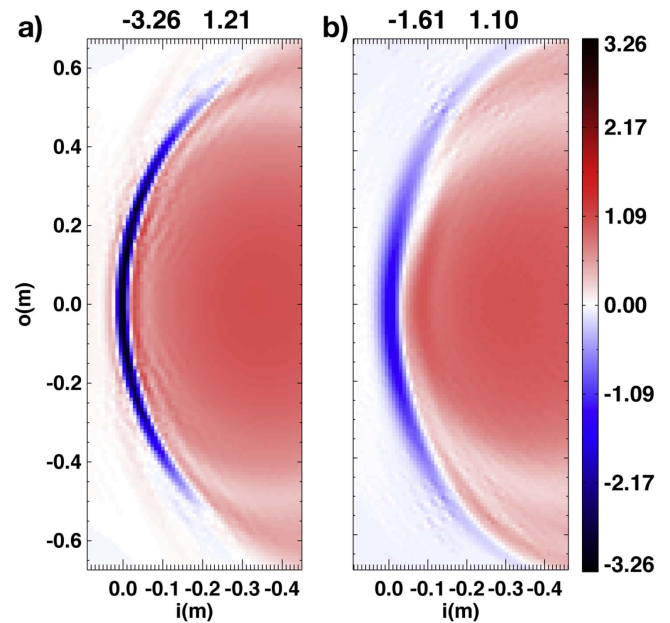

Figure 8. Helical current J_h in the reconnection plane for the (a) resistive-MHD and (b) extended-MHD simulations. The resistive current sheet is more elongated than in extended-MHD, as expected from Sweet–Parker theory.

measured a distance δ upstream, where δ is the location where J_h falls to half its maximum value in the inflow in a cut along $o = 0$. The current density in the out-of-plane (helical) direction J_h is shown in figure 8 for the (a) resistive-MHD and (b) extended-MHD simulations. The time slice for the extended-MHD simulation is well into the accelerated
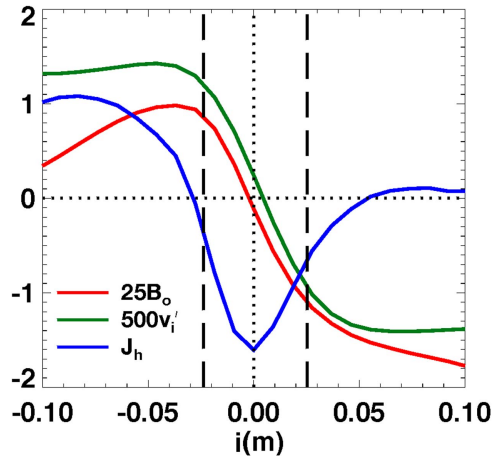
Figure 9. Profiles of the reconnecting field B_o, the inflow velocity v_i' (in the reference frame of the X-line), and the helical current J_h. Where J_h drops to half its maximum value is denoted by the vertical, dashed black lines; upstream quantities are evaluated there.

nonlinear phase $t = 1460$, and the resistive simulation has an island size comparable to that of the extended-MHD case at $t = 5625$. In each case, a strong thin current sheet is visible at the reconnection site. A comparison of the two simulations is carried out in the next subsection.

The thickness δ is measured along a cut at $o = 0$. Figure 9 shows J_h as a function of i for the extended-MHD simulation as the blue trace. The vertical dashed lines denote where J_h falls to half of its absolute maximum. This defines the thickness of the reconnection site in the inflow direction; the thickness for the extended-MHD simulation is $\delta = 0.0245$, and $\delta = 0.0135$ for the resistive-MHD simulation (not shown), and is where values of the upstream magnetic field and inflow speed are measured. Interestingly, due to our choice of η and d_b, the resistive current sheet is thinner than the extended-MHD current sheet, which may seem counter-intuitive. However, this actually should be expected and is a nice consistency check that extended-MHD physics are dominant in the extended-MHD simulation. It justifies our choice for η; if the width of the current sheet for the resistive simulation was larger than for the extended-MHD simulation, the extended-MHD effects would not have been active for the simulation with $d_b = 0.10$ [42]. For this scaled value of the ion inertial scale, the ion gyroradius based off the thermal speed $\rho_s = \sqrt{\beta/2}\, d_i = 0.015$ for the extended-MHD simulation, which is approximately $\delta/2$.

The cut of B_o is shown as the red trace (scaled up by a factor of 25 to be on the same axes). The upstream reconnecting magnetic field $B_{o,1}$ and $B_{o,2}$ are measured at the vertical dashed lines. The upstream inflow speeds $v_{i,1}$ and $v_{i,2}$ are measured at the same location. However, we note the reconnecting magnetic field B_o exhibits a weak asymmetry. When the magnetic fields are asymmetric, the X-line tends to move in the inflow direction towards the direction of stronger reconnecting magnetic field (the positive i direction, towards the tokamak edge) [43–48]. Thus, to get a proper

measurement of the reconnection parameters, we must measure the velocities in the reference frame of the moving X-line.

Transforming into the reference frame of the moving X-line is done using standard techniques [49, 50]. In the steady-state in quasi-2D systems, the reconnection electric field E_h' is uniform in the reference frame of the X-line, where we use a prime to denote quantities in the reference frame of the X-line. In the lab frame, the electric fields $E_{h,1} = v_{i,1}B_{o,1}$ and $E_{h,2} = v_{i,2}B_{o,2}$ differ. If the speed of the X-line is defined as $v_{i,X}$, then the reconnection electric field is $E_h' = (v_{i,1} + v_{i,X})B_{o,1} = (v_{i,2} - v_{i,X})B_{o,2}$. Solving these two equations for $v_{i,X}$ gives

$$v_{i,X} = \frac{E_{h,1} - E_{h,2}}{B_{o,1} + B_{o,2}}. \tag{13}$$

The calculated speed of the X-line from equation (13) are 1.2×10^{-4} and 2.6×10^{-3} for the resistive- and extended-MHD cases. We shift the inflow velocities accordingly to obtain v_i', the inflow in the reference frame of the X-line. This is plotted for the extended-MHD simulation in green in figure 9, scaled by a factor of 500 to be on the same axes.

We also measure the length of the reconnection region in the outflow direction in a similar manner as the width, except that the current sheet is curved. Thus, we find the location above and below the X-line at which the current density is half of its maximum, and calculate the distance along the current sheet to the X-line as L. For the extended-MHD simulation $L = 0.145$, and $L = 0.370$ for the resistive-MHD simulation. Since the current density is more strongly peaked near the X-line in the extended-MHD simulation, the length is shorter. We are now ready to quantitatively compare reconnection between resistive-MHD and extended-MHD simulations.

4.3. Local reconnection rates: resistive-versus extended-MHD

We first compare properties of the reconnecting current sheets visible in figure 8. The dominant feature is that the resistive current sheet is elongated compared to the extended-MHD current sheet. The resistive sheet has $\delta/L = 0.07$ compared to the extended-MHD sheet with $\delta/L = 0.17$. The extended-MHD result is in reasonable agreement with values seen in 2D slab geometry simulations, while resistive reconnection with smaller δ/L forms a nozzle which slows reconnection.

Next, we analyze profiles of the contributions to the out-of-plane electric field E_h' in Ohm's law (in the reference frame of the X-line) taken through the reconnection site in the inflow direction at $o = 0$. These profiles are shown in figure 10 for the (a) resistive- and (b) extended-MHD simulations. The asymmetric shift in the electric field is a consequence of the reconnection being asymmetric—the reconnecting fields and densities differ on the two sides [44]. Understanding the nature of this asymmetry in a torus should be the subject of future work as transport through the $q = 1$ surface is sensitive to the reconnection time [9], which is sensitive to the asymmetry (e.g. [44]).
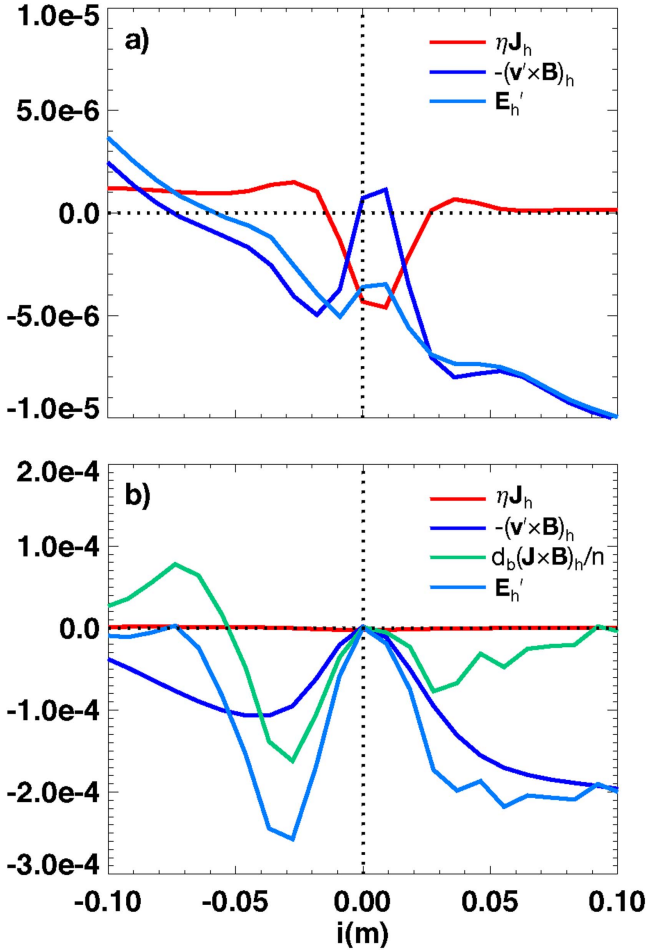
Figure 10. Profiles the out-of-plane component of the generalized Ohm's law taken through the reconnection site through $o = 0$ in the reconnection plane. (a) Resistive-MHD results, (b) extended-MHD results. The contribution due to the Hall term is visible in (b).

For the resistive simulation, the only terms that contribute are convection $-(v' \times \mathbf{B})_h$ and diffusion due to resistivity ηJ_h, shown by the dark blue and red lines respectively. The sum of the terms is E'_h, shown as the light blue line. They essentially balance (E'_h is relatively flat near the X-line), as one expects for steady-state 2D reconnection, with a local reconnection rate of about $E'_h \simeq 5 \times 10^{-6}$. The profiles are similar to those seen in 2D asymmetric reconnection in a slab geometry [44].

For the extended-MHD simulation, the dominant terms are convection and the Hall term $d_b (\mathbf{J} \times \mathbf{B})_h / n$ shown as the green line. The resistivity has a negligible contribution to E'_h, which is consistent with previous results (see, e.g., [26]). We find that the reconnection electric field is $E'_h \simeq 2 \times 10^{-4}$, ~40 times stronger than that of the resistive simulation. This shows the extended-MHD reconnection is faster, consistent with the known result that collisionless reconnection is much faster than resistive reconnection. Moreover, this result shows that the Hall term is contributing to the reconnection electric field near the X-line, showing that the numerical resolution in this region is sufficient.

We point out that the terms in Ohm's law shown in figure 10(b) are close to zero at the X-line. This is because in the extended-MHD simulation, the diffusive physics breaking the frozen-in condition is not resolved. In a real system, this effect is caused by electron inertia or off-diagonal elements of the electron pressure tensor. In this simulation without these effects, the mechanism breaking the frozen-in condition is undoubtedly numerical. Fortunately, the large scale properties of collisionless reconnection are insensitive to the physics breaking the frozen-in condition [51], so not resolving the artificial dissipation that breaks the frozen-in condition (which would be very computationally expensive) is not a detriment. Testing how the present results are affected when the dissipation mechanism is explicit as in [52] should be the subject of future work. In summary, we find that the local measure of the reconnection rate shows that extended-MHD is much faster than collisional reconnection, consistent with the global measures discussed earlier.

We now turn to a quantitative understanding of the local reconnection properties. First, as a consistency check, a by-product of the analysis leading to equation (13) is the reconnection electric field E'_h in the reference frame of the X-line. Using the values for the reconnecting field B_o and the inflow velocity v_i determined in the last section, we calculate the reconnection electric field (reconnection rate) [49, 50]:

$$E'_{h,meas} = \frac{E_{h,1} B_{o,2} + E_{h,2} B_{o,1}}{B_{o,1} + B_{o,2}}. \tag{14}$$

We find $E'_{h,meas} = 8.23 \times 10^{-5}$ for the extended-MHD simulation, which is within a factor of 2.5 of the value of $E'_h = 2 \times 10^{-4}$ obtained from figure 10(b), and $E'_{h,meas} = 3.30 \times 10^{-6}$ for the resistive-MHD simulation, which is within a factor of 1.5 of the value of $E'_h = 5 \times 10^{-6}$ obtained from figure 10(a).

Next, we employ analytical predictions to calculate the rate of reconnection and compare it to the measured value for the inboard reconnection site. A recent theory of 2D asymmetric reconnection in the absence of a guide field suggests [44]

$$E'_{h,pred} \sim \left(\frac{B_{o,1} B_{o,2}}{B_{o,1} + B_{o,2}} \right) v_{out} \frac{2\delta}{L}, \tag{15}$$

where v_{out} is the outflow speed from the reconnection site. For the extended-MHD simulation, using the measured value of $v_{out} = 0.021$, we get $E'_{h,pred} \sim 6.81 \times 10^{-5}$, which is within 20% of $E'_{h,meas}$. For the resistive-MHD simulation, using the measured value of $v_{out} = 0.00235$, we get $E'_{h,pred} \sim 3.33 \times 10^{-6}$, which agrees well with $E'_{h,meas}$. The agreement is quite good despite the fact that the theory is for 2D reconnection and does not treat the guide field or the curved magnetic geometry of a tokamak. This is simply for a single data point, so a more thorough study varying the plasma parameters is necessary before making any overarching conclusions, but the prediction does rather well for this simulation.

As a final quantitative check of the local reconnection rates, we compare the asymmetric Sweet–Parker reconnection
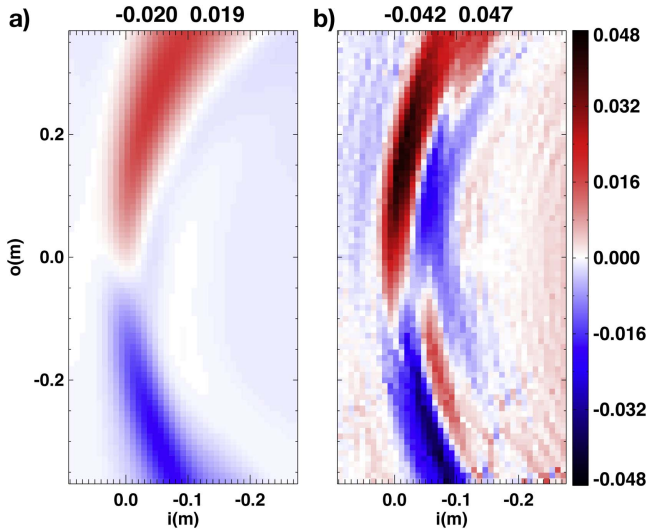
Figure 11. (a) Ion and (b) electron outflow speeds $v_{i,o}$ and $v_{e,o}$ in the reconnection plane located on the inboard side of the tokamak. Maximum electron flows are a factor of two larger than the ion flows and are peaked closer to the reconnection site.

Figure 12. (a) Toroidal magnetic field perturbation $\tilde{B}_\phi$ in the poloidal plane with the profile at the midplane subtracted out of every horizontal slice, leaving a dipolar structure. (b) Helical magnetic field perturbation $\tilde{B}_h$ in the reconnection plane with the profile through $o = 0$ subtracted out, which leaves a quadrupolar structure that has polarity consistent with collisionless reconnection due to the Hall term.

rate and current sheet width [44] to the previously measured and predicted values. The asymmetric Sweet–Parker reconnection rate is given by

$$E'_{SP} \sim \sqrt{\frac{\eta v_{out}}{L} B_{o,1} B_{o,2}}, \tag{16}$$

and is evaluated for the resistive-MHD simulation to give 3.93×10^{-6}, which agrees well with E'_h, $E'_{h,meas}$, and $E'_{h,pred}$. The half-widths of the current sheet on either side of the asymmetric reconnection layer are given by

$$\delta_{SP,1} \sim \sqrt{\frac{\eta L}{v_{out}} \frac{B_{o,1}}{B_{o,2}}}, \quad \delta_{SP,2} \sim \sqrt{\frac{\eta L}{v_{out}} \frac{B_{o,2}}{B_{o,1}}}, \tag{17}$$

and are evaluated for the resistive-MHD simulation to give $\delta_{SP,1} = 0.006$ and $\delta_{SP,2} = 0.026$, which agree well with the measured values of $\delta_1 = 0.008$ and $\delta_2 = 0.019$.

4.4. Separation of ion and electron scales in extended-MHD reconnection

Due to the disparity between the ion and electron masses, a characteristic feature of collisionless reconnection is a two-scale structure of the region near the X-line. In most cases, simulations purporting to capture extended-MHD effects on reconnection need resolution sufficient to resolve the separation in scales between ions and electrons. Shown in figure 11 are the outflow (o) components of the (a) ion velocity $\mathbf{v}_i$ and (b) electron velocity $\mathbf{v}_e$, where $\mathbf{v}_e = \mathbf{v}_i - (d_b/ne)J$. The maximum electron outflow speed is larger than that of the ions by over a factor of 2, consistent with extended-MHD and PIC slab reconnection studies (see, e.g., [53]).

Furthermore, the electron outflow jets are noticeably thinner than the ion outflow jets, consistent with the two-scale structure due to the inclusion of the Hall term in the generalized Ohm's law. While difficult to determine from the
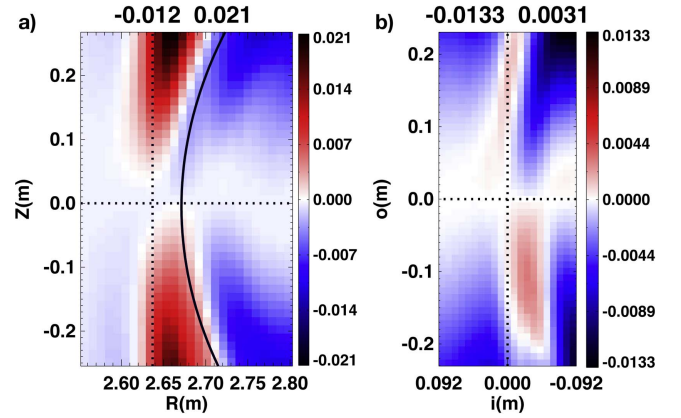
figure, the maximum electron velocity is peaked closer to the reconnection site than the maximum ion velocity, also consistent with known properties of collisionless reconnection [53]. These results suggest that extended-MHD physics is playing a role in these simulations as is expected, but has not previously been diagnosed in 3D toroidal simulations.

An interesting observation is that both the ion and electron flows are in the direction of the electron diamagnetic drift velocity v_{*e} at the reconnection site, which is consistent with the 2D slab simulations [23, 54]. This suggests that electron diamagnetic effects are playing a role in the local flow dynamics at the reconnection site, a phenomena that will be the subject of future study.

4.5. Identification of the hall magnetic field

An important signature of collisionless reconnection is the existence of a quadrupole in the out-of-plane magnetic field [55, 56]. It has been observed experimentally in satellite observations (see, e.g., [49]) and in dedicated reconnection experiments (see, e.g., [57]). However the small reconnection scales in a tokamak makes viewing this structure prohibitively difficult. Furthermore, to the best of our knowledge, it has not been identified in fully 3D toroidal simulations until now.

We first show the toroidal magnetic field in the poloidal $(R - Z)$ plane at the inboard side of the torus. Since the background $B_\phi \propto 1/R$ dominates the signal, a meaningful measure of the role of the Hall term would remove the background. To handle this, we define the perturbed toroidal magnetic field $\tilde{B}_\phi$ as the full B_ϕ with the profile of B_ϕ at the midplane ($Z = 0$) subtracted from every slice of constant Z. This is plotted for the extended-MHD simulation in figure 12(a). The dotted lines mark axes through the location of the reconnection site as determined from the Poincaré plot. The solid line shows the calculated $q = 1$ surface from averaging over the magnetic field in the toroidal and poloidal directions, where the difference from the Poincaré method

Table 2. Measured characteristic values of extended-MHD reconnection, where the reconnection site is located at different toroidal (and poloidal) angles. Tabulated values are the reconnecting magnetic field in the inflows toward the core and edge $B_{o,core}$ and $B_{o,edge}$, the density n at the X-line, the average ion outflow velocity $v_{i,out,ave}$, the average electron outflow velocity $v_{e,out,ave}$, the total length of the current sheet $2L$, and the total thickness of the current sheet 2δ.

Location	$B_{o,core}$	$B_{o,edge}$	n	$v_{i,out,ave}$	$v_{e,out,ave}$	$2L$	2δ
Outboard	0.02	0.014	0.83	0.028	0.063	0.45	0.051
Top	0.044	0.01	0.91	0.025	0.059	0.28	0.048
Inboard	0.034	0.044	1.1	0.021	0.047	0.29	0.049
Bottom	0.024	0.038	0.95	0.024	0.051	0.35	0.057

reveals the non-axisymmetry of the mode. From this figure, it is evident that there is no quadrupolar field signature in $\tilde{B}_\phi$ when viewed from the poloidal plane.

However, in the reconnection plane, we define a similarly calculated perturbed helical magnetic field $\tilde{B}_h$, where the B_h profile through $o = 0$ has been subtracted off all cuts at fixed o. The result is shown in figure 12(b); we find a quadrupolar perturbed helical magnetic field. From the polarity of the in-plane magnetic fields as shown in figure 7, the polarity of the quadrupole out-of-plane field is consistent with that of the expected Hall magnetic field. Note, the quadrupole $\tilde{B}_h$ is not observed in the reconnection plane of the resistive-MHD simulations (not shown). These results are indicative that the Hall term is actively playing a role in the extended-MHD simulation, corroborating the result in figure 10.

The helical (guide) field is strong compared to the relatively weak reconnecting field, with a ratio of $\bar{B}_o/B_h \simeq 0.039/1.23 = 3.2\%$, where $\bar{B}_o$ is the average of B_o on the two sides of the reconnection site. For reconnection with a strong guide field, it is expected that the helical quadrupole field is accompanied by a quadrupole gas pressure profile in order to maintain total pressure balance [58]. Interestingly, we find no gas pressure quadrupole in the reconnection plane for this extended-MHD simulation. Additionally, the ratio of the quadrupolar field to the reconnecting field departs from predictions that $\tilde{B}_h \sim B_o$ [59]. We hypothesize that the curved geometry of the toroidal system and extremely large B_h/B_o ratio implies that additional physics due to magnetic field bending be kept in the scaling relations; this analysis is left for a future study. In summary, we have shown evidence local to the reconnection site that Hall reconnection takes place.

5. Toroidal dependence

Thus far, the discussion has been limited to the reconnection site located on the inboard side of the torus. In this section we explore how reconnection changes for different toroidal angles, where the reconnection site is located at different poloidal locations. However, we continue to look at data in the reconnection plane as opposed to the poloidal plane. In what follows, we compare the reconnection planes for the toroidal locations where the X-line is on the inboard, top, outboard, and bottom of the $q = 1$ rational surface. We limit

our analysis to the extended-MHD simulation, but comment that the results are similar for the resistive-MHD simulation.

Using the methodology in section 4.2, we find upstream values representing the reconnection process. We find the reconnecting magnetic fields in the inflows of the core $B_{o,core}$ and the edge $B_{o,edge}$, the density at the X-line, the ion and electron outflow speeds $v_{i,out,ave}$ and $v_{e,out,ave}$ averaged over the two jets, the full length of the current sheet $2L$, and the full width of the current sheet 2δ. Measured parameters are listed in table 2.

For perspective, we show the structure of the reconnecting current sheet J_h in figure 13. The reconnection sites are on the (a) inboard, (b) top, (c) outboard, and (d) bottom of the $q = 1$ rational surface as determined from Poincaré plots. We note that there is some numerical noise towards the inboard side, which we attribute to the modest toroidal resolution; a convergence study of the toroidal resolution will be a matter for future work. The principal feature is that the maximum J_h at different toroidal angles is greater on the inboard side, and is smaller on the outboard side. This is expected because the toroidal field varies as $B_\phi \sim 1/R$, leading to stronger reconnecting fields B_o towards the inboard side. Then, since the width of the current sheet is set by the reconnection physics, we expect the current density to be largest on the inboard side, consistent with our simulations.

The average ion and electron flows are the smallest on the inboard side where the density is largest; this is consistent with the reconnection outflows scaling with the Alfvén speed $\propto n^{-1/2}$. There is a toroidal variation in the length of the current sheet, which we attribute to toroidal geometry. Using figure 6 for a helical field line with a circular cross-section as a reference, the path length from the top to the bottom on the inboard side is shorter than the path length connecting the top and bottom on the outboard side because B is stronger on the inboard side. The width of the current sheet δ varies only slightly with toroidal (poloidal) location.

We now turn to quantifying the local reconnection rate at the four toroidal locations. Table 3 contains the aspect ratio of the reconnection region δ/L, the measured helical electric field E'_h, and the calculated reconnection electric fields $E'_{h,meas}$ and $E'_{h,pred}$ from equations (14) and (15), respectively. Since L increases towards the outboard side due to the toroidal geometry, δ/L decreases, implying that reconnection proceeds more slowly towards the outboard side of the tokamak. The decrease in the rate of reconnection toward the outboard side
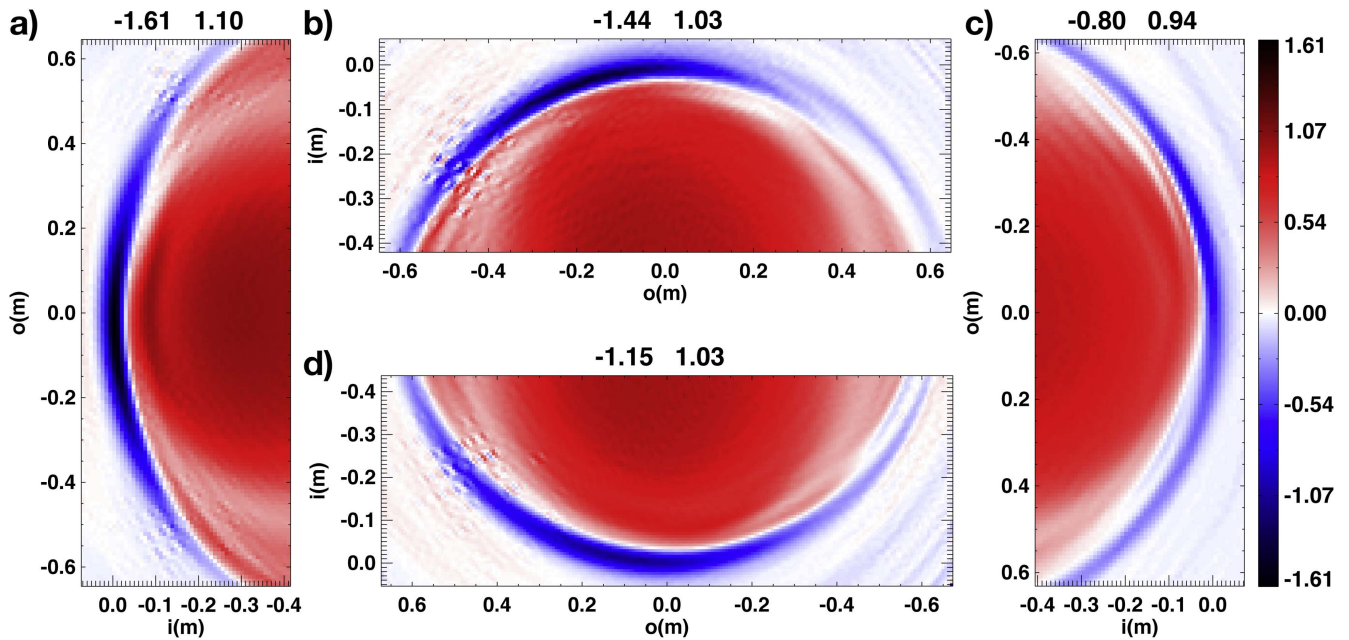
Figure 13. Views of the helical reconnection current density J_{h} in the reconnection plane at different toroidal angles corresponding to where the reconnection site is at the (a) inboard, (b) top, (c) outboard, and (d) bottom of the torus. The maximum magnitude of the reconnection current is on the inboard side, where the toroidal field is the strongest. Also, δ/L is greater towards the inboard side, and lower towards the outboard side.

Table 3. Aspect ratio of the reconnection site δ/L, measured E_{h}' and calculated $E_{\mathrm{h,meas}}'$ and $E_{\mathrm{h,pred}}'$ values of the reconnection rate at the same four locations as in table 2. $E_{\mathrm{h,meas}}'$ is calculated using equation (14) and $E_{\mathrm{h,pred}}'$ is calculated using equation (15).

Location	δ/L	E_{h}'	$E_{\mathrm{h,meas}}'$	$E_{\mathrm{h,pred}}'$
Outboard	0.11	7.3×10^{-5}	2.6×10^{-5}	2.6×10^{-5}
Top	0.17	1.0×10^{-4}	2.3×10^{-5}	3.4×10^{-5}
Inboard	0.17	2.0×10^{-4}	8.2×10^{-5}	6.8×10^{-5}
Bottom	0.16	1.4×10^{-4}	6.5×10^{-5}	5.7×10^{-5}

is also visible in the electric field measurements and calculations.

Another interesting aspect is that reconnection at the top and bottom is asymmetric in the outflow direction. In figure 13, the inboard and outboard current sheets are mostly centered around the midplane, but the top and bottom current sheets are shifted towards the inboard side of the torus. This is also apparent from looking at the ion outflow jets, shown in figure 14 for the (a) top and (b) bottom reconnection sites. The faster outflow jets are toward the outboard side for both sites. This asymmetry in the outflow jets can be explained by the toroidal magnetic field dependence in the major radial direction, decreasing as $\sim 1/R$. At the inboard and outboard reconnection sites, the toroidal magnetic field changes through the inflow direction, contributing to the helical current, but at the top and bottom sites the toroidal magnetic field changes through the outflow direction. There are very few papers studying reconnection that is asymmetric in the outflow direction. One showed that if there is a gas pressure
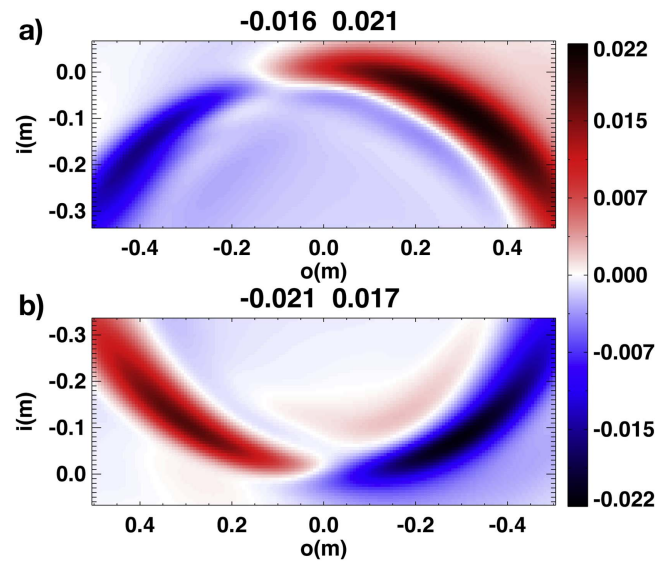

Figure 14. Ion outflow speed v_{o} when the reconnection site is at the (a) top and (b) bottom of the rational surface. The outflows are asymmetric due to the magnetic pressure gradient in the major radial direction due to the varying toroidal magnetic field.

gradient in the outflow direction, there is an outflow asymmetry with the faster outflow where the gas pressure is less [60]. Similarly here, there is a magnetic field pressure gradient towards the inboard side of the torus, and for the top and bottom sites this gradient is in the outflow direction, consistent with the polarity of the asymmetric outflows.

Interestingly, the simulations reveal an asymmetry of the electron temperature for the top and bottom reconnection
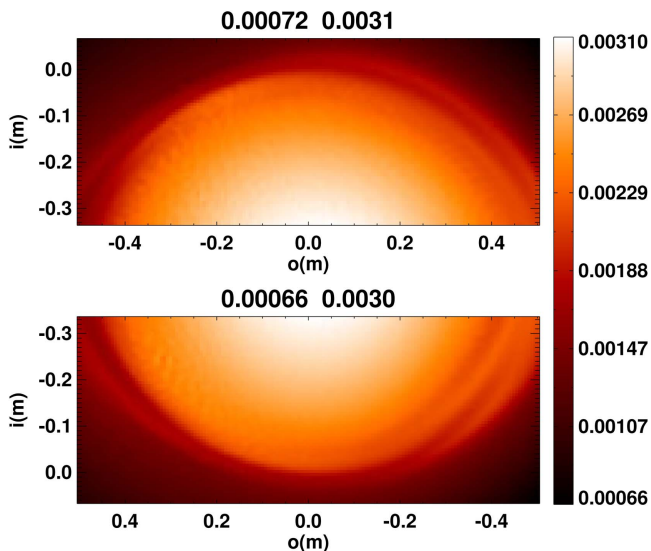
Figure 15. Electron temperature T_e in the reconnection plane when the reconnection site is at the (a) top and (b) bottom. Consistent with the results of [30], the hot core bulges toward the outboard side of the torus.

sites, as seen in figure 15. The temperature in the outflow jet directed toward the outboard side is greater than that in the outflow jet toward the inboard side. This gives the appearance that the high temperature core is offset toward the outboard side. This is consistent with the experimental result of [30], where the hot core was shifted toward the outboard side when the sawtooth mode was on the top and bottom sides of the tokamak.

6. Conclusions and discussion

6.1. Conclusions

It has long been known that reconnection in sawteeth occurs in the auxiliary plane normal to the helical magnetic field at the $q = 1$ surface, and idealized simulations of reconnection in cylindrical geometries have taken this into account. However, we are not aware of any simulation studies in fully 3D toroidal geometries that study reconnection in the reconnection plane. This study has carefully and systematically devised an approach for analyzing reconnection in a 3D toroidal geometry in the plane of reconnection.

We use Poincaré plots and plasma profiles to find the reconnection X-line in a particular poloidal plane. Then, we find the helical direction at that point, and the reconnection plane is normal to the helical direction. We orient the plane with vectors spanning the plane and develop a technique to automatically identify the inflow and outflow directions.

We utilize the extended-MHD code M3D-C^1, to perform a systematic study of the local reconnection properties and to compare the results of between resistive-MHD and extended-MHD simulations. Globally, we find that the growth of the kinetic energy in different toroidal modes for the extended-MHD reconnection process is substantially greater than in

resistive-MHD and exhibits a nonlinear acceleration, with crash times more consistent with experimental results. This is consistent with the hypothesis that collisionless reconnection is necessary to explain observed crash times.

We observe toroidal rotation due to the externally applied neutral beam, which causes poloidal rotation of the helical mode during the longer timescale of the resistive simulation, consistent with experimental results [30]. During the tearing phase in the extended-MHD simulations, the tearing site drifted in the direction of v_{*e}, which shows that the magnetic field configuration drifts with the electron diamagnetic flow. This poloidal drift is consistent with the initial findings of [1], which reported that the sawtooth mode propagates in the v_{*e} direction. This will be the topic of future work.

By sampling the extended-MHD simulation data in the plane perpendicular to the local magnetic field at the reconnection site, we confirm the approach we developed successfully found the reconnection plane. We find the local parameters controlling the reconnection (in the moving reference frame of the X-line), find the non-ideal contributions to Ohm's law which become important in the reconnection region, directly measure the reconnection electric field and show it is in reasonable agreement with a 2D prediction, show the decoupling of the electrons and ions in the region near the reconnection site, and show the first observation of the quadrupole out-of-plane magnetic field resulting from the Hall term in collisionless reconnection.

We also explored how reconnection varies with toroidal (and poloidal) angle, which is an interesting aspect that has not received much attention but is relevant because $q = 1$ magnetic field lines wrap around the rational surface and sample local parameters varying from the inboard to outboard sides. Reconnection is faster on the inboard side even though the outflow speeds are higher on the outboard side. We posit that toroidal geometry affects the aspect ratio of the reconnection geometry, elongating the reconnection site on the outboard side. The varying toroidal magnetic field causes an outflow asymmetry on the top and bottom of the torus. Because these asymmetries and current sheet variations alter the rate of reconnection, this is important for understanding how the reconnection mode evolves locally throughout the tokamak.

6.2. Discussion

The results of this study are important results for a number of reasons. First, with regard to the role of collisionless effects in the sawtooth crash, the approach employed here provides a systematic approach to confirm given numerical results are properly resolving the appropriate physics. The approaches employed here were only tested on simulation results from a single code, but the approach is general and should work with any 3D toroidal simulation output. Second, by demonstrating how to measure local properties of reconnection, it enhances our ability to study the reconnection process in sawteeth in tokamaks, which is important for developing a first-principles understanding. Since sawteeth are crucial for transport and current transport models employ ad hoc techniques to

incorporate sawtooth crash times, such a research direction is very important.

The present results show that local 2D reconnection models agree reasonably well with reconnection properties in the fully 3D toroidal geometry, which suggest that such an approach can be useful for predicting quantitative behavior of tokamak reconnection-related phenomena.

The study of the toroidal angle variation of reconnection could be useful for analysis of experimental data, such as recent work in [30]. While the WT-3 tokamak is no longer in use, there has been recent installations of quasi-3D electron cyclotron emission diagnostics on the Korea Superconducting Tokamak Advanced Research [61] and ASDEX-U [62] tokamaks. The local reconnection analysis utilized in this paper could be directly tested on either device. This local analysis could also be useful for modeling and analyzing reconnection events occurring during non-inductive startup in many spherical tokamaks, including MAST [63], NSTX-U [64], and Pegasus [65].

The local reconnection analysis could also be valuable for diagnosing other dynamic events in tokamaks that involve magnetic reconnection, namely, NTMs and the use of resonant magnetic perturbations (RMPs) to suppress edge localized modes (ELMs). An understanding of the suppression of ELMs by RMPs will also lead to knowledge of the edge confinement degradation known as density pumpout. A detailed understanding of both NTM and RMP processes are of major importance to the success of future fusion devices, and an understanding of the local reconnection dynamics at the higher order rational surfaces where these processes occur is essential.

As mentioned throughout the text, there are several limitations of the present study that should be addressed in future work. Convergence tests on the poloidal and toroidal resolution for the extended-MHD simulation shown are needed. One could include an explicit, higher-order numerical magnetic diffusivity to control the dissipation mechanism breaking the frozen-in condition at the reconnection X-point. Future work should apply the local reconnection analysis across test simulations with different equilibrium magnetic and thermal profiles, and especially across experimental data, moving past the test simulation used here. One could also revisit the analytic theory of asymmetric reconnection to include a guide magnetic field, curved geometry effects, and a drifting reference frame. A more thorough understanding of what controls the structure and amplitude of the out-of-plane (helical) Hall quadrupole field structure when including curved geometry and drift effects would be useful. The effects on sawtooth reconnection due to diamagnetic drifts will be discussed in a forthcoming paper.

Acknowledgments

References

[1] von Goeler S, Stodiek W and Sautoff N R 1974 *Phys. Rev. Lett.* **33** 1201
[2] Kadomtsev B B 1975 *Fiz. Plazmy* **1** 710
[3] Wesson J A 1986 *Plasma Phys. Control. Fusion* **28** 243
[4] Hender T C *et al* 2007 *Nucl. Fusion* **47** S128
[5] Bhatnagar V, Start D, Jacquinot J, Chaland F, Cherubini A and Porcelli F 1994 *Nucl. Fusion* **34** 1579
[6] Petty C C, Austin M E, Holcomb C T, Jayakumar R J, La Haye R J, Luce T C, Makowski M A, Politzer P A and Wade M R 2009 *Phys. Rev. Lett.* **102** 045005
[7] Sips A C C *et al* 2002 *Plasma Phys. Control. Fusion* **44** B69
[8] Jardin S C, Ferraro N and Krebs I 2015 *Phys. Rev. Lett.* **115** 215001
[9] Muscatello C M, Heidbrink W W, Kolesnichenko Y I, Lutsenko V V, Zeeland M A V and Yakovenko Y V 2012 *Plasma Phys. Control. Fusion* **54** 025006
[10] Sauter O *et al* 2002 *Phys. Rev. Lett.* **88** 105001
[11] Wesson J 1987 *Tokamaks* (Oxford: Clarendon)
[12] Sykes A and Wesson J A 1976 *Phys. Rev. Lett.* **37** 140
[13] Denton R, Drake J F, Kleva R G and Boyd D 1986 *Phys. Rev. Lett.* **56** 2477
[14] Edwards A W *et al* 1986 *Phys. Rev. Lett.* **57** 210
[15] Yamada M, Levinton F M, Pomphrey N, Budny R, Manickam J and Nagayama Y 1994 *Phys. Plasmas* **1** 3269
[16] Aydemir A Y 1992 *Phys. Fluids* B **4** 3469
[17] Porcelli F, Boucher D and Rosenbluth M N 1996 *Plasma Phys. Control. Fusion* **38** 2163
[18] Bateman G, Nguyen C N, Kritz A H and Porcelli F 2006 *Phys. Plasmas* **13** 072505
[19] Holmes J A, Carreras B A and Charlton L A 1989 *Phys. Fluids* B **1** 788
[20] Kleva R G 1992 *Phys. Fluids* B **4** 218
[21] Wang X and Bhattacharjee A 1995 *Phys. Plasmas* **2** 171
[22] Kleva R G and Guzdar P N 2002 *Phys. Plasmas* **9** 3013
[23] Beidler M T and Cassak P A 2011 *Phys. Rev. Lett.* **107** 255002
[24] Breslau J A, Jardin S C and Park W 2007 *Phys. Plasmas* **14** 056105
[25] Park W, Belova E V, Fu G Y, Tang X Z, Strauss H R and Sugiyama L E 1999 *Phys. Plasmas.* **6** 1796
[26] Günter S, Yu Q, Lackner K, Bhattacharjee A and Huang Y-M 2015 *Plasma Phys. Control. Fusion* **57** 014017
[27] Yu Q, Günter S and Lackner K 2015 *Nucl. Fusion* **55** 113008
[28] Yu Q 2010 *Nucl. Fusion* **50** 025014
[29] Pontin D I 2011 *Adv. Space Res.* **47** 1508
[30] Yamaguchi S, Igami H, Tanaka H and Maekawa T 2004 *Plasma Phys. Conrol Fusion* **46** 1163
[31] Ferraro N M and Jardin S C 2009 *J. Comput. Phys.* **228** 7742
[32] Braginskii S I 1965 *Rev. Plasma Phys.* **1** 205
[33] Jardin S C 2004 *J. Comput. Phys.* **200** 133
[34] Breslau J, Ferraro N and Jardin S 2009 *Phys. Plasmas* **16** 092503
[35] Jardin S C 2012 *J. Comput. Phys.* **231** 822
[36] Grad H and Rubin H 1958 *Proc. 2nd UN Conf. on the Peaceful Uses of Atomic Energy* vol 31 (IAEA) p 190
[37] Shafranov V D 1966 *Rev. Plasma Phys.* **2** 103
[38] Jardin S C, Ferraro N, Breslau J and Chen J 2012 *Comput. Sci. Discovery* **5** 014002

[39] Biskamp D, Schwarz E and Drake J F 1997 *Phys. Plasmas* **4** 1002
[40] Parnell C E, Haynes A L and Galsgaard K 2010 *J. Geophys. Res.* **115** A02102
[41] Komar C M and Cassak P A 2016 *J. Geophys. Res.* **121** 5105
[42] Cassak P A, Shay M A and Drake J F 2005 *Phys. Rev. Lett.* **95** 235002
[43] Ugai M 2000 *Phys. Plasma* **7** 867
[44] Cassak P A and Shay M A 2007 *Phys. Plasmas* **14** 102114
[45] Cassak P A and Shay M A 2008 *Geophys. Res. Lett.* **35** L19102
[46] Hoshino M and Nishida A 1983 *J. Geophys. Res.* **88** 6926
[47] Scholer M 1989 *J. Geophys. Res.* **94** 15099
[48] Rijnbeek R P, Semenov V S, Shmalts A A, Biernat H K, Heyn M F and Besser B P 1991 *Planet. Space Sci.* **39** 1377
[49] Mozer F, Bale S D and Phan T D 2002 *Phys. Rev. Lett.* **89** 015002
[50] Cassak P A and Shay M A 2009 *Phys. Plasmas* **16** 055704
[51] Birn J *et al* 2001 *J. Geophys. Res.* **106** 3715
[52] Jardin S, Breslau J and Ferraro N 2007 *J. Comput. Phys.* **226** 2146
[53] Shay M A, Drake J F, Denton R E and Biskamp D 1998 *J. Geophys. Res.* **25** 9165
[54] Swisdak M, Drake J F, Shay M A and Rogers B N 2003 *J. Geophys. Res.* **108** 1218
[55] Sonnerup B U Ö 1979 *Solar System Plasma Physics* (vol 3) ed L J Lanzerotti, C F Kennel and E N Parker (Amsterdam: North-Holland) p 46
[56] Mandt M E, Denton R E and Drake J F 1994 *Geophys. Res. Lett.* **21** 73
[57] Yamada M, Ren Y, Ji H, Breslau J, Gerhardt S, Kulsrud R and Kuritsyn A 2006 *Phys. Plasmas* **13** 052119
[58] Kleva R, Drake J and Waelbroeck F 1995 *Phys. Plasma* **2** 23
[59] Rogers B N and Denton R E 2003 *J. Geophys. Res.* **108** 1111
[60] Murphy N A, Sovinec C R and Cassak P A 2010 *J. Geophys. Res.* **115** A09206
[61] Yun G S *et al* 2014 *Rev. Sci. Instrum.* **85** 11D820
[62] Classen I G J, Domier C W, Luhmann N C, Bogomolov A V, Suttrop W, Boom J E, Tobias B J and Donné A J H ASDEX Upgrade Team 2014 *Rev. Sci. Instrum.* **85** 11D833
[63] Stanier A, Browning P, Gordovskyy M, McClements K G, Gryaznevich M P and Lukin V S 2013 *Phys. Plasmas* **20** 122302
[64] Ebrahimi F, Hooper E B, Sovinec C R and Raman R 2013 *Phys. Plasmas* **20** 090702
[65] O'Bryan J B and Sovinec C R 2014 *Plasma Phys. Control. Fusion* **56** 064005